PNAS RESEARCH ARTICLE | ENGINEERING
BIOPHYSICS AND COMPUTATIONAL BIOLOGY

# Molecular understanding of $Ni^{2+}$-nitrogen family metal-coordinated hydrogel relaxation times using free energy landscapes

Eesha Khare[a,b], Seth Allen Cazzell[a], Jake Song[a], Niels Holten-Andersen[a,c,1], and Markus J. Buehler[b,1]

Edited by Zhiping Xu, Tsinghua University, Beijing, China; received August 1, 2022; accepted December 20, 2022 by Editorial Board Member Yonggang Huang

**Incorporating dynamic metal-coordination bonds as cross-links into synthetic materials has become attractive not only to improve self-healing and toughness, but also due to the tunability of metal-coordination bonds. However, a priori determination of bond lifetime of metal-coordination complexes, especially important in the rational design of metal-coordinated materials with prescribed properties, is missing. We report an empirical relationship between the energy landscape of metal-coordination bonds, simulated via metadynamics, and the resulting macroscopic relaxation time in ideal metal-coordinated hydrogels. Importantly, we expand the Arrhenius relationship between the macroscopic hydrogel relaxation time and metal-coordinate bond activation energy to include width and landscape ruggedness identified in the simulated energy landscapes. Using biologically relevant $Ni^{2+}$-nitrogen coordination complexes as a model case, we demonstrate that the quantitative relationship developed from histidine-$Ni^{2+}$ and imidazole-$Ni^{2+}$ complexes can predict the average relaxation times of other $Ni^{2+}$-nitrogen coordinated networks. We anticipate the quantitative relationship presented here to be a starting point for the development of more sophisticated models that can predict relaxation timescales of materials with programmable viscoelastic properties.**

## Significance

Transition-metal bonds are emerging for use in engineering advanced dynamic, tunable, and reversible (e.g., self-healing) mechanical properties, due to their capacity to reform after rupture compared with traditional covalent bonds. A framework to effectively predict the properties of these bonds would significantly help future design and incorporation of these bonds in new materials. In this work, using molecular dynamics, we quantitatively relate the simulated energy landscape of metal-coordination bonds in hydrogels to the experimentally measured macroscopic relaxation time of metal-coordinated hydrogel networks. We show how this relationship can predict the relaxation time of other chemically similar metal-coordinated networks. This work is a critical advance in helping provide tools for a priori design of dynamic materials.

Some biological materials enriched in metal-coordination bonds, such as the mussel byssal thread, display simultaneous autonomous self-healing and high toughness, properties that are often traded off in synthetic materials. (1, 2) Inspired by such biological materials, researchers have incorporated metal-coordination bonds into synthetic polymer and protein-based materials to induce desirable mechanical properties, including high fracture toughness, self-healing, stimuli-responsive dynamic behavior, and dampening. (3–8) These dynamic mechanical properties are enabled by the lability of metal-coordination bonds, which can break and reform over mechanically relevant time and temperature scales. As such, incorporation alongside permanent loadbearing bonds in macromolecular networks enables metal-coordination bonds to act as sacrificial bonds, breaking instead of permanent bonds that keep the structural integrity of the material intact. Further, metal-coordination bonds are highly tunable—simply exchanging the metal ion, ligand, or solvent involved in coordination can dramatically affect the dynamic properties of these bonds by changing bond strength and dissociation rate. (3)

The dynamics of metal-coordination bonds are intimately coupled to their local microscopic environment, making their smart incorporation into synthetic materials nontrivial. For example, despite the extensive metal-coordination found in both marine mussel threads and marine worm jaws, the marine mussel thread is adhesive, soft, and tough, whereas the marine worm jaw is hard, stiff, and fracture resistant, differences in material properties likely caused by distinctive protein structures and levels of hydration. A fundamental understanding of the microscopic origin of the macroscopic behavior of metal-coordinate cross-linked materials would enable better utilization of metal-coordination bonds in the future design of loadbearing materials.

Molecular modeling methods offer an opportunity to elucidate the microscopic origin of metal-coordinate bond behavior. Xu and Vidavsky et al. used first-principles calculations to correlate the strength of a coordination complex to the macroscopic stiffness of a metal-coordinated polymer network. (9, 10) Li et al. also used first-principles calculations to compute force-displacement data to compare against experimental single molecule force spectroscopy data on coordination bonds. (11) Others have also proposed relationships between bond strength and macroscopic material strength. (12) However, these approaches have focused primarily on static properties, or strength of coordination complexes, rather than dynamic bond properties that significantly affect time-dependent macroscopic material properties, which also have important effects on toughness, stretchability, and self-healing. The computational exploration of metal-coordination bond dynamics is a new frontier and is especially challenging due to the limitations of conventional metal ion force fields and long sampling methods needed to probe relevant timescales.

Author contributions: E.K., N.H.-A., and M.J.B. designed research; E.K., S.A.C., and J.S. performed research; E.K., S.A.C., J.S., N.H.-A., and M.J.B. contributed new reagents/analytic tools; E.K., S.A.C., J.S., N.H.-A., and M.J.B. analyzed data; and E.K., S.A.C., J.S., N.H.-A., and M.J.B. wrote the paper.

The authors declare no competing interest.

This article is a PNAS Direct Submission. Z.X. is a Guest Editor invited by the Editorial Board.



[1]To whom correspondence may be addressed. Email: nih221@lehigh.edu or mbuehler@mit.edu.

This article contains supporting information online at https://www.pnas.org/lookup/suppl/doi:10.1073/pnas.2213160120/-/DCSupplemental.

Published January 17, 2023.

In this work, we report the microscopic behavior of metal-coordination bonds using simulated free energy landscapes and quantify how this energy landscape relates to dynamic mechanical properties of a bulk metal-coordinate cross-linked material. Selecting biologically relevant metal-coordinate complexes imidazole-$Ni^{2+}$ and histidine-$Ni^{2+}$ as a demonstration model system, we correlate bond lifetimes estimated from simulations of coordination complexes with experimentally measured bulk network relaxation times of ideal-network metal-coordinated gels. (6) Through a quantitative empirical relationship, we show how the energy landscape of individual coordination bonds can be related to the macroscopic viscoelastic behavior of metal-coordinated polymer networks, despite their vastly different time and length scales of investigation (Fig. 1). Specifically, we discuss how key features of the metal-coordinate bond energy landscape may contribute to bulk gel relaxation time, and we use these features to expand the conventional Arrhenius equation to predict the relaxation time of other $Ni^{2+}$-nitrogen-containing metal-coordination chemistries in ideal networks. This study empirically relates the energy landscape of metal-coordinate bonds with the macroscopic dynamic mechanical behavior of metal-coordinated hydrogels and posit a quantitative empirical relationship between bond energy landscape and bulk network relaxation time. The methodology and insights developed here pave the way for further studies on both the detailed chemical mechanisms of metal-coordinate bond breaking and a priori prediction of viscoelastic properties for metal-coordinated hydrogels.

## Results

**Dynamic Behavior of $Ni^{2+}$-Nitrogen Family Hydrogels.** As a demonstration model system, we focus on the $Ni^{2+}$-nitrogen family (imidazole and histidine) complexes due to their prevalence in biology and the development of appropriate $Ni^{2+}$ force fields. This focus is also in large part inspired by the original study on histidine-metal coordinate cross-linking in hydrogels by Fullenkamp et al., which documented that coordination cross-links involving histidine, but not imidazole, lead to more solid-like hydrogels. (5) Both histidine and imidazole ligands are nitrogen-containing chelators with similar structures. Imidazole consists of a five-membered heterocycle where the pyridine-like nitrogen coordinates in a monodentate interaction to metal ions under basic conditions. Histidine consists of the same imidazole heterocycle and an additional amine group, which can also coordinate metal ions, thereby composing a more stable bidentate interaction (Fig. 2, *Inset*), as originally proposed by Fullenkamp et al.

To isolate the mechanical effect of these stereochemical differences in metal-coordinating ligands, we incorporated imidazole and histidine as telechelic ligands in 4-arm-PEG polymers and established hydrogel networks cross-linked via $Ni^{2+}$ ions. To maximize the mechanical signal-to-noise ratio of metal–ligand dissociation, we employ nearly ideal polymer networks in a regime below entanglements (see calculations in the *SI Appendix*), such that bulk relaxation time of the network is dominated by the kinetics of the dynamic metal–ligand cross-links. (6, 13, 14)

As demonstrated in Fig. 2, 4-arm-PEG-histidine hydrogel networks display a bulk relaxation time ($\tau$) of $\tau \sim 400$ s, whereas 4-arm-PEG-imidazole networks display a $\tau \sim 0.06$ s at 5 °C based on a Maxwell model fit. This observation supports the hypothesis that the monodentate imidazole-$Ni^{2+}$ bond acts as a more labile cross-link, whereas bidentate histidine-$Ni^{2+}$ bond results in a slower cross-link dissociation rate in synthetic hydrogels. A similar large difference in dissociation rates between nearly identical metal-coordinating ligands has been observed for other stereochemistries, (15) but a mechanistic explanation for these differences remains speculative.

**Free Energy Landscapes of $Ni^{2+}$-Nitrogen Coordination Complexes.** To better understand the effect of ligand stereochemistry and local chemical environment on dissociation rate, or inversely bond lifetime, of the coordination complexes, the free energy landscapes of histidine and imidazole coordinating with $Ni^{2+}$ ions were characterized via metadynamics. Metadynamics enables a computationally efficient evaluation of energy landscapes via the addition of bias potentials that overcome local minima. (16–18) To ensure a relevant comparison between experiment and simulation, we first determined which metal-coordinate complexes would be dominant in the hydrogels using thermodynamic equilibrium predictions that use bond chemistry and hydrogel pH to calculate species distributions of coordinate complexes (*SI Appendix*, Fig. S1) (19). Based on these calculations, we proceeded with computing the free energy landscapes of the dominant $His_2Ni_1$ and $Im_2Ni_1$ complexes, representing two histidine or imidazole ligands coordinated with one $Ni^{2+}$, in water solvated environments.

The selection of an appropriate reaction coordinate, or collective variable (CV), is critical in calculating an energy landscape, which captures all relevant reactants, products, and intermediate states. For this simulation, the CVs are chosen as distance between $Ni^{2+}$ and the center-of-mass of the coordinating nitrogen atoms on each ligand (*SI Appendix*, Fig. S2). The free energy landscapes are illustrated in Fig. 3 *A* and *B*. Note that the key features of the free

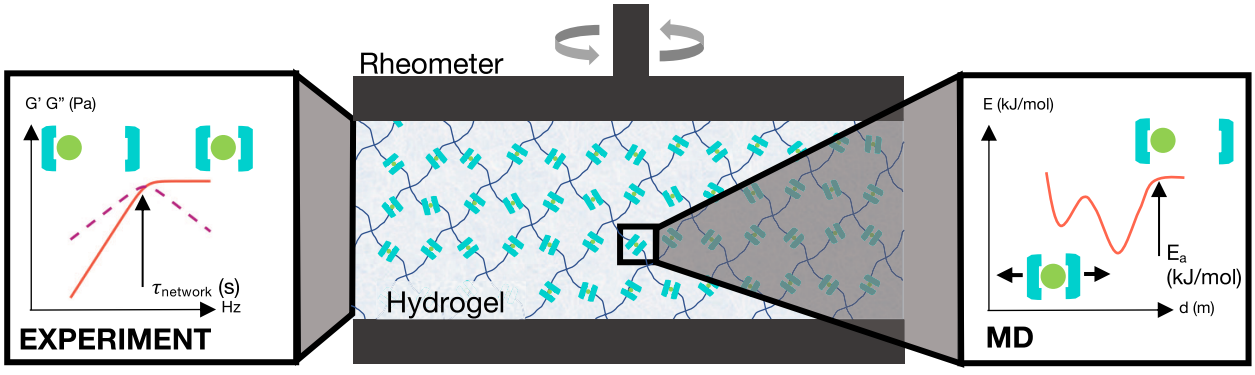


**Fig. 1.** Time and length scales in simulation and experiment. The macroscopic network relaxation time ($\tau$) of the hydrogel can be experimentally measured via a frequency sweep with a rheometer. This network relaxation time measurement is an experimental manifestation of the collective dissociation and reassociation dynamics of all loadbearing metal-coordination bonds within the network. MD simulation calculates the energy landscape of an individual metal-coordination bond, through which bond lifetime can be inferred.

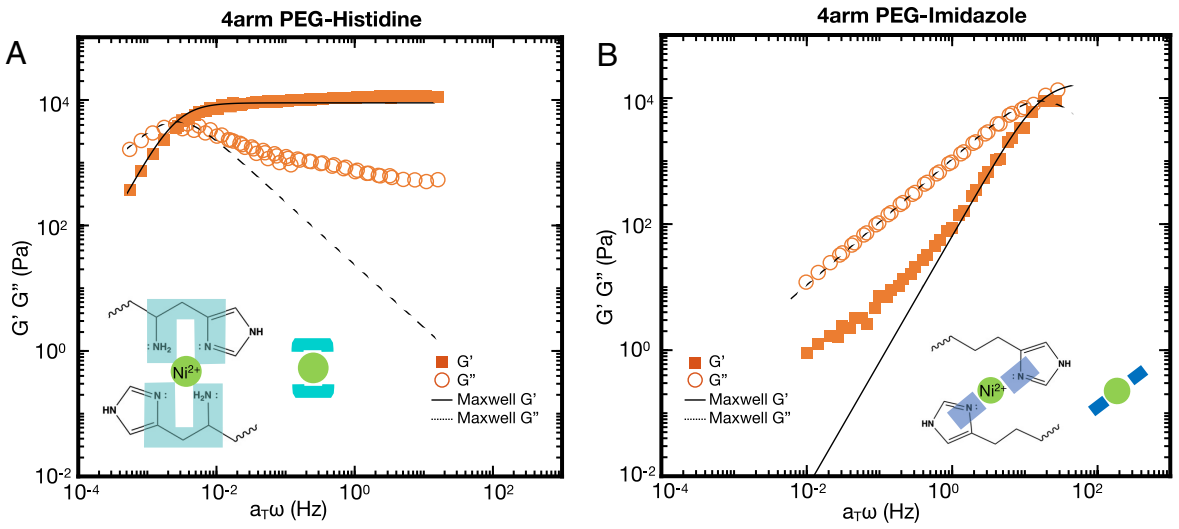


**Fig. 2.** 4PEG-histidine gels are slower relaxing than 4PEG-imidazole gels. Time-temperature superpositioned storage (*G'*) and loss moduli (*G''*) at 5 °C from frequency sweeps collected over several temperatures for (*A*) 1M:2L ratio of $Ni^{2+}$ –4arm PEG-histidine and (*B*) 1M:2L ratio of $Ni^{2+}$ –4arm PEG-imidazole at ~pH 8 at ~20% w/v. Schematic of dominant coordination complex in each gel based on equilibrium predictions is shown in insets. Each gel demonstrates Maxwellian behavior, with imidazole gels deviating in the low-frequency regime likely due to the broader speciation of coordination complexes present in imidazole gels compared with histidine gels (*SI Appendix*, Fig. S1).

energy landscapes of coordination complexes conjugated to PEG-polymer are preserved when compared with the free energy landscapes of coordination complexes alone (*SI Appendix*, Fig. S3). Thus, the free energy landscapes of the polymer-conjugated coordination complexes were not simulated further because their large size requires significantly more simulation time.

Compared with $Im_2Ni_1$, $His_2Ni_1$ displays a deeper energy well by ~40 kJ/mol indicating stronger binding between histidine and $Ni^{2+}$ than between imidazole and $Ni^{2+}$, as originally hypothesized by Fullenkamp et al. The lowest energy binding state is captured in Fig. 3 *A* and *B* and represents either four nitrogen atoms and two nitrogen atoms binding to $Ni^{2+}$ for histidine and imidazole, respectively (*SI Appendix*, Fig. S2). $His_2Ni_1$ also demonstrates a metastable binding state where three nitrogen atoms coordinate to $Ni^{2+}$.

**Predicting Macroscopic Network Dynamics from the Energy Landscape.** To compute quantitative parameters on the energy landscape surface, we compute the minimum energy path, which is the parametric curve that connects two energy minima on the energy landscape surface while using the shallowest ascent to traverse the minimum energy barrier between the two minima (Fig. 3 *A* and *B*, red, and black lines). The minima are selected to be the fully associated state, where two ligands are bound to one metal ion, and the dissociated state, where one ligand is dissociated from the metal-coordinate complex while the other ligand remains bound. This minimum energy path from the fully associated to a dissociated state represents the microscopic event hypothesized as the origin of the macroscopic relaxation process of the metal-coordinated network. (20, 21) Notably, the minimum energy path (Fig. 3 *A*–*D*, red, and black lines) is almost exactly the same as the reaction path where one ligand dissociates while the other remains bound to the metal ion at a fixed distance, which would be perfectly horizontal or vertical lines on the energy landscape. Along this reaction path, we can compute the bond dissociation activation energy ($E_a$) (Fig. 3*D*), which plays a critical role in determining relaxation time through an Arrhenius dependence (Eq. **S1**).

Crucially, we find that despite the large differences in length and time scales probed in simulation on an individual metal-coordinate complex and in experiment on a metal-coordinated hydrogel network, the estimated $E_a$ barriers governing the system dynamics on both the micro- and macroscopic scales follow the same ordering when comparing across different coordination complexes (Fig. 4*A*). Specifically, $His_2Ni_1$ has a higher $E_a$ in simulation than $Im_2Ni_1$ by ~7 kJ/mol. This is consistent with the slower experimentally measured bulk relaxation time of histidine-$Ni^{2+}$ as opposed to imidazole-$Ni^{2+}$ coordinated networks.

However, differences in $E_a$ between $His_2Ni_1$ and $Im_2Ni_1$ alone are unable to account for the large magnitude of difference in relaxation time between the histidine-$Ni^{2+}$ and imidazole-$Ni^{2+}$ hydrogels (*SI Appendix*, Fig. S4). Our simulated energy landscapes allow us to access other critical parameters along the ligand dissociation pathways that may contribute to the observed differences in relaxation timescales.

As such, we propose a simple heuristic relationship using key features of the microscopic energy landscape to explain macroscopic network relaxation time. The parameters are selected based on key observable differences between the energy landscapes of $His_2Ni_1$ and $Im_2Ni_1$. One parameter selected is the Gaussian width ($r_{Gaussian}$, as shown in Fig. 3*D*) of the deepest binding energy well. $r_{Gaussian}$ serves as a proxy for bond stiffness, where a larger $r_{Gaussian}$ implies a less stiff bond. $r_{Gaussian}$ is normalized by the metal–ligand bond length at break ($r_{break}$, as shown in Fig. 3*D*) to result in the dimensionless functional form $W$ representing bond stiffness.

$$W = \frac{r_{\text{Gaussian}}}{r_{\text{break}}} \quad [1]$$

In addition to the large differences in $E_a$ and $W$, $His_2Ni_1$ has more local minima around the deepest binding energy well than $Im_2Ni_1$ (Fig. 3 *A* and *B*). As we will discuss in the next section, these additional minima can be interpreted as metastable binding states, which may also contribute to the longer bond lifetime of $His_2Ni_1$ compared with $Im_2Ni_1$. We express these additional minima, or ruggedness $R$, using the dimensionless number of Fourier terms that fit the local minima in the landscape (as shown in Fig. 3*C*).

Building on the Arrhenius relationship for τ, we include the above stated $W$ and $R$ to yield the following proposed equation for average network relaxation time:

$$\tau \sim b_1 + b_2 \times e^{\frac{Ea}{kT}} + b_3 \times W^{b_4} + b_5 \times R^{b_6} \quad [2]$$

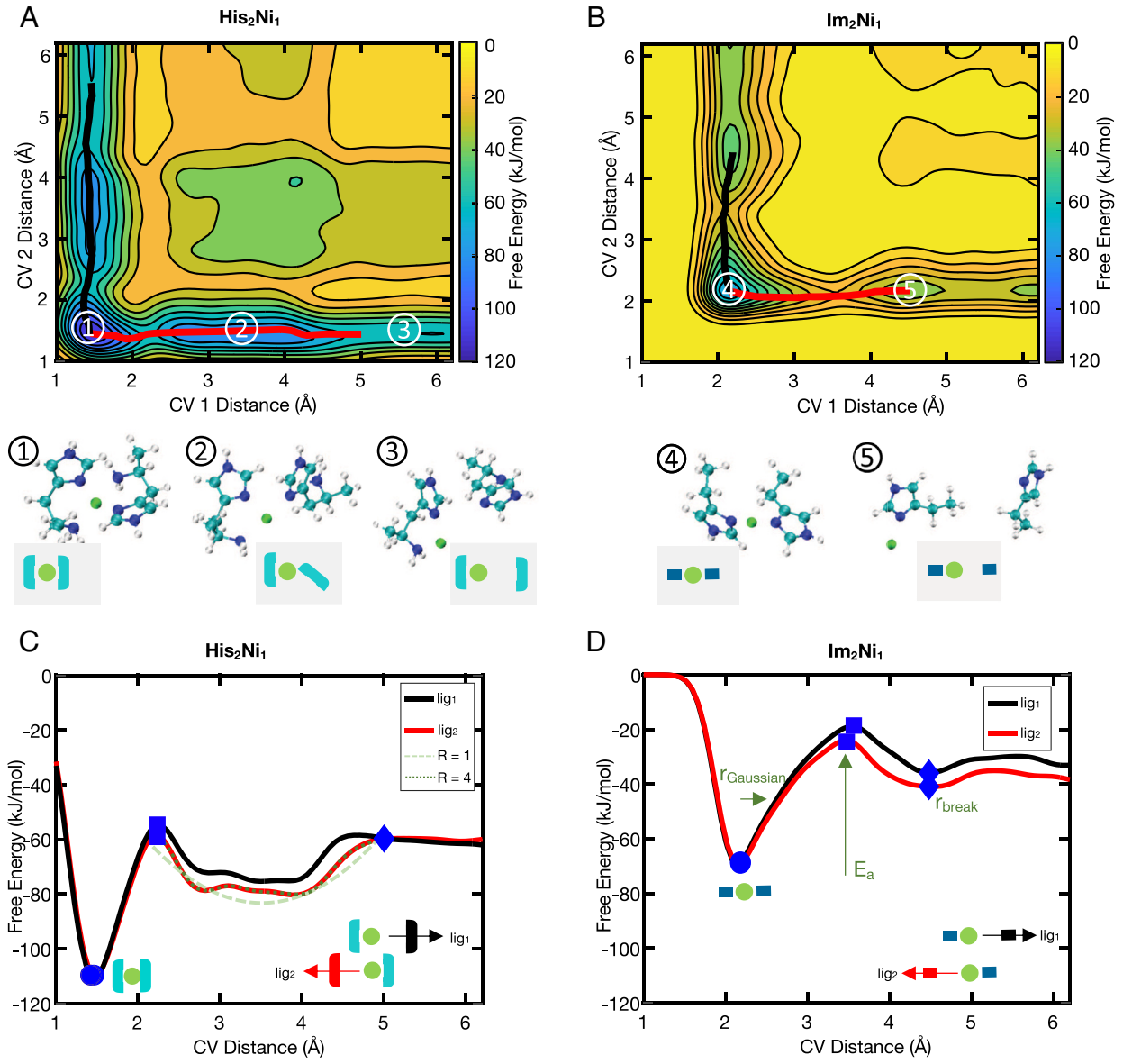


**Fig. 3.** Free energy landscapes of $His_2Ni_1$ and $Im_2Ni_1$ complexes demonstrate clear differences in energies and shape. Free energy landscape of two (*A*) histidine and (*B*) imidazole ligands bound with $Ni^{2+}$ with the CVs of the metadynamics simulation plotted as the X and Y-axes. $His_2Ni_1$ has a narrower and deeper well than $Im_2Ni_1$, indicating more stable coordination complex binding. Inset demonstrates schematics of the binding state of the coordination complexes with the atomistic representations drawn above. Red and black path lines are the minimum energy ligand dissociation path from the lowest energy minima (fully bound state) to the next energy minima (dissociated state with one ligand dissociated). The minimum energy paths are almost entirely parallel with the axes, representing the physical phenomena where one ligand is bound to the metal ion at a constant distance while the other dissociates. This ligand dissociation path is also the microscopic event hypothesized as the origin of the macroscopic relaxation process of the metal-coordinated network. The minimum energy path can be further visualized as 2D energy landscapes for (*C*) $His_2Ni_1$ and d) $Im_2Ni_1$ where for the legend entry "$lig_1$," $lig_2$ is held constant while $lig_1$ dissociates and "$lig_2$" is vice versa (see *Inset*). The landscape is described by $E_a$, R, and W. (*C*) R is the minimum number of Fourier terms that best fit the metastable well (dashed lines). (*D*) The activation energy ($E_a$) is computed as the difference between the minimum energy (blue circle) and highest transition energy (blue square) before the bond is broken (blue diamond). W is the Gaussian fitting distance ($r_{Gaussian}$) divided by the distance at break ($r_{break}$). $His_2Ni_1$ has a larger R and $r_{break}$ and smaller $r_{Gaussian}$ than $Im_2Ni_1$

By fitting the coefficients of this equation using the $E_a$, $W$ and $R$ of $His_2Ni_1$ and $Im_2Ni_1$ (*SI Appendix*, Table S1), we find the coefficients listed in *SI Appendix*, Table S2. Here the coefficients ($b_2$, $b_3$, $b_5$) represent intrinsic times associated with each aspect, $E_a$, $W$, and $R$, respectively, of the energy landscape. The scaling factors ($b_1$, $b_4$, $b_6$) capture time and length scale differences in MD and experiment.

$\tau$ increases exponentially with $E_a$ as already expected from the Arrhenius equation (Fig. 4*B*). We find that $\tau$ has a direct relationship with the number of local minima, likely because coordinate complexes such as $His_2Ni_1$ with additional local minima have more complex dissociation mechanisms, which thereby increase lifetime (Fig. 4*C*). Further, we find that $\tau$ has a direct relationship with $W$, indicating that a wider bond potential has a longer bond lifetime (Fig. 4*D*). Interestingly, $\tau$ is more sensitive to changes in $R$ than $W$ indicating that the number of metastable states plays a greater role in controlling relaxation time. Given this relationship, we show that for a given activation energy, chosen here as that of $His_2Ni_1$, the range of relaxation times can vary significantly based on ruggedness and bond stiffness (Fig. 4*E*). The effect of ruggedness and bond stiffness using the activation energy of $Im_2Ni_1$ is further shown in *SI Appendix*, Fig. S5.

The above empirical relationship enables a more facile a priori prediction of bulk relaxation times using the computational

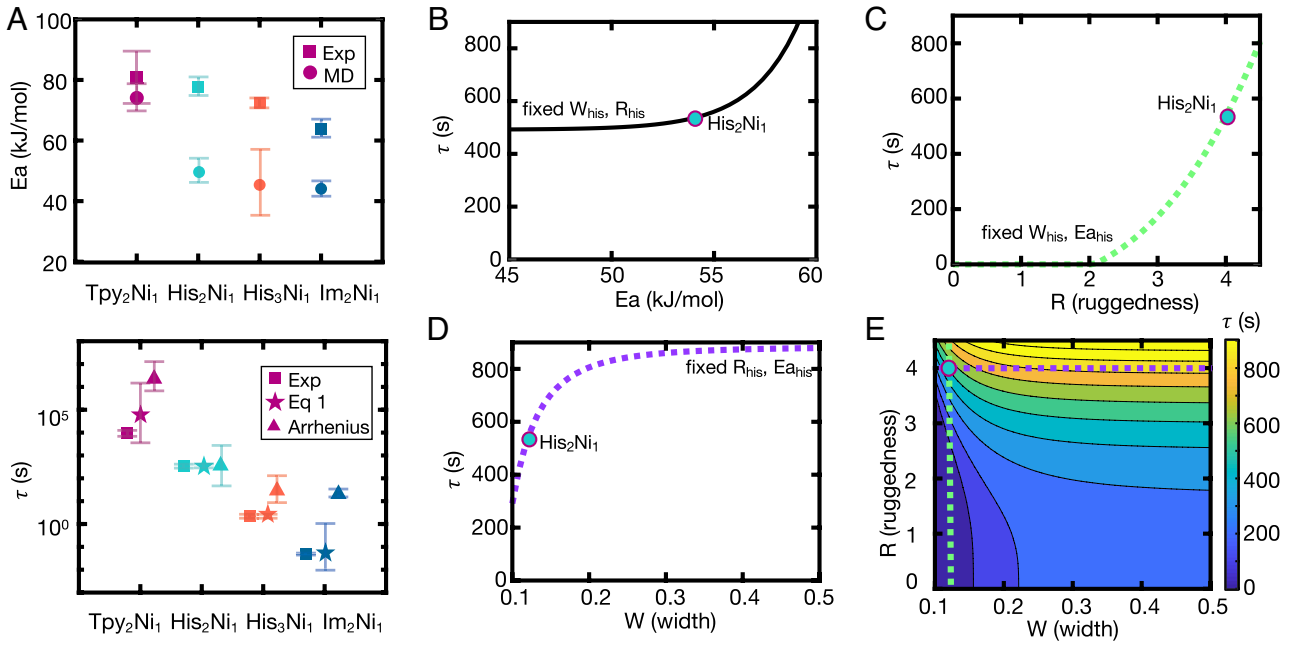


**Fig. 4.** Comparison between experiment and simulation show matching qualitative trends and an empirical relationship. (*A*) Experimental relaxation time, experimental activation energy, and simulated activation energies follow the same qualitative trends. The order of terpyridine $Tpy_2Ni_1$ > $His_2Ni_1$ > $His_3Ni_1$ > $Im_2Ni_1$ kinetic stability is preserved in both experiment and simulation, even though experimental observations are made on a macroscopic polymer network with coordination complexes and simulation is based on a single coordination complex. The triangles represent the relaxation times predicted by the Arrhenius relationship alone (*SI Appendix*, Fig. S4), and the stars represent the relaxation times predicted by Eq. **1**. Note some error bars are very small and difficult to visualize. Effects of (*B*) $E_a$ (*C*) R or (*D*) W on relaxation time (τ) are plotted when the other two independent variables (W and R, $E_a$ and W, or $E_a$ and R of $His_2Ni_1$, respectively) are held constant. (*B*) τ increases exponentially with $E_a$. (*C*) τ increases with R. (*D*) τ increases asymptotically with W. Plotted points represent the τ given the $E_a$, W, and R of $His_2Ni_1$. (*E*) Given a fixed $E_a$ of $His_2Ni_1$, τ can be varied significantly with changing width (W) and landscape ruggedness (R).

techniques demonstrated in this paper. We probed whether we could use our characterization of the microscopic $His_2Ni_1$ and $Im_2Ni_1$ energy landscapes to predict the macroscopic behavior of networks cross-linked with other $Ni^{2+}$-nitrogen-containing ligands, such as terpyridine (Tpy), a tridentate ligand, or other metal-ligand stoichiometries, such as $His_3Ni_1$. Remarkably, we find that Eq. **1** predicts the relaxation time of a $His_3Ni_1$ network to be $\tau \sim 3$ s and $Tpy_2Ni_1$ to be $\tau \sim 1 \times 10^5$ s which is reasonably consistent within the same order of magnitude as our experiments (*SI Appendix*, Figs. S6 and S7).

## Discussion and Conclusions

Selecting $Ni^{2+}$-nitrogen family coordination complexes as a demonstration model system, we have shown how 4-arm-PEG-histidine and imidazole $Ni^{2+}$-coordinated networks differ in macroscopic relaxation times and how that difference is reflected in the energy landscapes of the coordination complexes $His_2Ni_1$ and $Im_2Ni_1$. Though histidine and imidazole differ by one coordinating nitrogen, when incorporated as load-bearing cross-links in ideal polymer networks, they produce vastly different network relaxation times by a factor of ~6,000. In our simple 4-arm-PEG-imidazole hydrogels, imidazole-$Ni^{2+}$ cross-links are too labile to produce stable solid-like networks at room temperature. The lability of imidazole-$Ni^{2+}$ in hydrogels is surprising because imidazole is a key ligand in coordinating with metal ions in proteins where it provides greater structural stability.(3, 22–24) In proteins however, higher order protein structure may position imidazole ligands to enable stable cross-links with metal ions. When taken out of this molecular context, the additional amine coordination provided by histidine is necessary for solid-like gel formation, as demonstrated by Fullenkamp et al. (5)

Our simulations indicate that this vast difference in histidine and imidazole's $Ni^{2+}$-coordinated network relaxation times may be correlated to several differences in the microscopic energy landscapes of their dominant coordination complexes $His_2Ni_1$ and $Im_2Ni_1$. First and foremost, as originally proposed based on an assumed Arrhenius-dependent relationship between network relaxation time and the energy barrier to ligand dissociation, we show that $His_2Ni_1$ indeed has a much deeper binding well with a higher bond dissociation activation energy than $Im_2Ni_1$. Further, $His_2Ni_1$ has additional metastable states, likely due to a more complex dissociation mechanism than $Im_2Ni_1$. The existence of metastable states is similar to protein folding energy landscapes that have several local minima, which often help guide specific folding pathways or regulate folding dynamics. (25) Like in these protein systems, the additional metastable minima in the polymer hydrogel may help slow relaxation dynamics. Potentially, these metastable wells may also enable the ligands to partially dissociate and then reassociate quickly to help in recovering the fully bound coordination complex. This hypothesis could be examined further in future work as an area of exploration, similar to the relationship between local minima in the energy landscape and material recovery suggested in Sun et al. (12)

Using these key energy landscape features that distinguish histidine from imidazole, we posited that the relaxation time of the experimental metal-coordinated network can be empirically calculated through an expanded Arrhenius equation that not only includes activation energy, but also bond stiffness, and number of local minima—all microscopic parameters determined from the energy landscape. Each of these microscopic parameters lends critical insights into the effect of energy landscape on coordination bond lifetime. As already established with the traditional Arrhenius equation, a larger bond dissociation activation energy results in a longer lifetime. Further, we find that a less stiff bond results in a longer lifetime, which aligns with Kramers' escape rate theory discussed in the following paragraph where a less stiff, or wider bond width, results in a longer time. The additional local minima

also contribute to extending lifetime by enabling different configurations of the ligand–metal ion binding. Not only does the empirical relationship developed in this work lend insight into how different energy landscape parameters affect bond lifetime, but it also enables a priori predictions of relaxation times of other similar metal-coordinated gels. Here, the empirical relationship developed from $His_2Ni_1$ and $Im_2Ni_1$ allow us to predict the network relaxation time of $His_3Ni_1$ and $Tpy_2Ni_1$ reasonably.

We emphasize again that we are proposing an empirical relationship for the microscopic energy landscape and macroscopic relaxation time, rather than a physicochemical theory. This is in part due to limitations with metal ion force fields that currently do not fully capture details of metal-ligand charge transfer. (26–28) Given this limitation, we focus on the empirical relationship here as it serves our intended purpose: to both predict relaxation times for other nitrogen-based ligands coordinating with $Ni^{2+}$ and observe the effects of different landscape parameters on bond lifetimes. We also considered other classical rate models, (29) such as Kramers' theory about the escape of a particle over an energy potential barrier, as a basis for our quantitative relationship. The detailed discussion of theories considered in model development is in the *SI Appendix*. More simulations, theory, and improved metal ion force fields are needed to derive a detailed physicochemical relationship between energy landscapes and resulting bond lifetimes beyond the empirical relationship proposed here.

The microscopic energy landscape of the individual coordination complex is also only one critical component in the determination of the macroscopic relaxation time of ideal metal-coordinated networks. Despite the ideal nature of the hydrogel network, there are still heterogeneous structures and defects that contribute to the network relaxation behavior. (30) Though the coefficients and scaling factors in Eq. **1** capture some of these network-related dynamics effects, additional mesoscale simulations would be required to include network heterogeneity to resemble real hydrogels more closely and probe the resulting range of relaxation times over an ensemble of simulations. More detailed quantum chemical simulations of these coordination complexes may also further help bridge the differences in $E_a$ between MD on the single coordination complexes and experiment on coordination networks (Fig. 4*A*).

This work dissects an energy landscape of a bond and relate it to experimental macroscopic kinetics of a system. The framework developed here opens several areas of exploration for designing materials with a better understanding of how bond chemistries affect dynamic macroscopic properties. We strongly believe our approach to the demonstration model system of $Ni^{2+}$-nitrogen family of coordination complexes will be relevant to other coordination bond chemistries and more complex chemical environments, such as the metal-coordination bonds within the protein structure of the mussel thread and marine worm jaw, to better characterize their natural energy landscapes. Next steps can be taken to explore the relevance of Eq. **1** to other coordination bond chemistries with better metal ion force field development. Such mechanistic insights hold the potential to guide the a priori design of metal-coordinated materials with specific relaxation times toward useful biological viscoelastic tissue mimics and self-healing sustainable construction materials.

## Methods

**Synthesis of 4PEG-Histidine.** 4PEG-His was synthesized using modifications of the procedure by Cazzell et al. (19) Briefly, 3 g 4-arm 10 kDa PEG-NH2·HCl (0.25 equiv of PEG, 1.0 equiv of −NH2 groups) (JenKem USA) was mixed with Boc-His(Trt)-OH (1.5 equiv) and BOP reagent (1.5 equiv) and dissolved in ~10 mL dichloromethane. N,N-Diisopropylethylamine (DIPEA) (535 equiv) was added, and the reaction was allowed to proceed overnight under $N_2$. The product was purified by precipitation once in diethyl ether, thrice in methanol at −20 °C, and once in diethyl ether. The product was then dried under vacuum. Protecting groups were removed by a cleavage cocktail of 95 mL trifluoroacetic acid, 2.5 mL triisopropylsilane, and 2.5 mL $H_2O$ for 2 h. An equal volume of methanol was then added, and the solvent was removed using a rotary evaporator. The final product was purified by dissolving it in methanol and precipitation in ether three times and vacuum drying. $^1$H NMR (500 MHz, CDCl3) δ 8.67 (s, 4H), 7.43 (s, 4H), 4.44 (t, 4H), 3.89–3.33 (m, 848H), 3.29 (t, 8H). Coupling efficiency estimated to be 82%. See *SI Appendix*, Fig. S8 for characterization data.

**Synthesis of 4PEG-Imidazole.** 4PEG-Im was synthesized using modifications of the procedure by Fullenkamp et al. (5) Briefly, 3 g 4-arm 10 kDa PEG-$NH_2$·HCl (0.25 equiv of PEG, 1.0 equiv of −$NH_2$ groups) (JenKem USA) was mixed with 3-(N-1-Trityl- imidazol-4-yl) propionic acid (0.69 g, 1.8 mmol, Chem-Impex International, Inc.) (1.5 equiv) and BOP reagent (1.5 equiv) and dissolved in ~10 mL dimethylformamide. N,N-Diisopropylethylamine (DIPEA) (535 equiv) was added, and the reaction was allowed to proceed overnight under $N_2$. The product was purified by precipitation once in diethyl ether, thrice in methanol at −20 °C, and once in diethyl ether. The product was then dried under vacuum. Protecting groups were removed by a cleavage cocktail of 95 mL trifluoroacetic acid, 2.5 mL triisopropylsilane, and 2.5 mL $H_2O$ for 2 h. An equal volume of methanol was then added, and the solvent was removed using a rotary evaporator. The final product was purified by dissolving it in methanol and precipitation in ether three times and vacuum drying. $^1$H NMR (500 MHz, $CDCl_3$) δ 8.61 (s, 4H), 7.76 (s, 4H), 3.89-3.33 (m, 848H), 3.05 (s, 8H), 2.69 (s, 8H). Coupling efficiency estimated to be 78%. See *SI Appendix*, Fig. S8 for characterization data.

**Synthesis of 4PEG-Terpyridine.** Synthesis of 4PEG-Terpyridine. 4PEG-Tpy was synthesized in the following manner. N-[3-([2,2′:6′,2″-terpyridin]-4′-yloxy)-propyl]methacrylamide precursors were first synthesized following modifications of the protocol (40). Briefly, 3 g powdered KOH was dissolved in 224 mL of DMSO in a flask at 40 °C, after which 6 mL of 3-aminopropanol was added dropwise to the heated mixture. After 20 minutes, 5 g 4′-chloro-2,2′:6′,2″-terpyridineis added to the flask under N2, and the reaction was allowed to proceed for 2.5 hours. The mixture was then poured into excess deionized water and left in a -20 °C freezer overnight to precipitate. The resulting precipitates were removed by vacuum filtration, washed again in deionized water, and vacuum dried. Next, 1 g of 4-arm 10 kDa PEG-NHS (JenKem USA) was mixed with the synthesized terpyridyl-4-oxy-propylamine (0.17 g) at a molar ratio of 6:1, and dissolved in 3 mL of DMSO under N2, followed by the addition of 0.1 mL of TEA. The reaction was allowed to proceed at 60 °C overnight. The mixture was then poured into acetone and left in a -20 °C freezer overnight to precipitate. The precipitates were removed by vacuum filtration, washed in diethyl ether, and vacuum dried. 1H NMR (500MHz, (CD3)2SO) 8.75–8.60 (m, 4H), 8.03-7.87 (m, 4H), 7.52-7.48 (m,2H), 3.60-3.45 (m, 848H), 3.32 (s, 8H). Coupling efficiency estimated to be 85%. See *SI Appendix*, Fig. S8 for characterization data.

**Hydrogel Formation.** Hydrogels were formed by modifying the method described elsewhere. (19) At a concentration of 400 mg/mL, 4-arm PEG polymer was dissolved in 18.2 MΩ cm water. Then, 50 μL of this solution was dispensed onto Parafilm®. 0.2 M nickel (II) chloride hexahydrate was added to achieve the appropriate metal-to-ligand stoichiometry. 1 M sodium hydroxide was then added to reach the final pH, and the resulting mixture was then homogenized by mixing with the spatula and by kneading the material by folding the Parafilm®. The final concentration of the gel was ~20% w/v, which is above critical overlap concentration and below the entanglement as confirmed by us and others (see *SI Appendix* for calculations). (13, 31) The observed relaxation times are well above $\tau_{chain}$ (13).

**Experimental Testing of Hydrogel.** The resulting hydrogels were measured for their viscoelastic properties and pH. The gels were loaded onto an MCR 302 stress-controlled rheometer from Anton Paar and tested using a 10-mm diameter parallel plate. Frequency sweeps were performed from 100 to 0.1 rad/s at temperatures from 0 to 35 °C at a strain amplitude of 1%, within the linear viscoelastic regime of histidine and imidazole gels. After the 35 °C frequency sweep, a strain sweep was performed from 0.01% to 1,000% strain at a frequency of 1 Hz to confirm the linear viscoelastic regime of the gels at 5 °C (*SI Appendix*, Fig. S9). Time temperature superposition was used to combine the frequency

sweep results for various temperatures referenced to 5 °C. The plateau modulus was determined as the maximum value of the storage modulus, and the relaxation time was determined from the cross-over of the storage and loss modulus using a Maxwell fit. The pH of the gels was determined using a SoilStik pH meter from FieldScout.

**Computational Modeling of Energy Landscapes.** MD simulations implemented in LAMMPS (32) are used to investigate the energy landscape of imidazole, histidine, and pyridine ligands using the CHARMM22 force field (33, 34). $Ni^{2+}$ metal ion parameters from Babu and Lim are used as they simultaneously replicate relative hydration free energies, first-shell coordination numbers, and average water–ion distances. (35) PEG parameters from the CHARMM c35r ether force field are used as they replicate persistence length, hydrodynamic radii, and scaling of radius of gyration with molecular weight well. (36) The ligands and metal ion are solvated in a 50 Å × 50 Å × 50 Å water box using TIP3P water molecules. Solvated ligands are equilibrated using an NPT ensemble with a constant pressure of 1 atm at 300 K for 2 ns followed by equilibration with an NVT ensemble for 1 ns using the Nose/Hoover thermostat and barostat. A simulation timestep of 2 fs was chosen with a cutoff for nonbonded interactions at 12 Å. The particle-particle-particle-mesh (PPPM) method (37) was used to compute the long-range columbic interactions and the SHAKE algorithm (38) was applied to constrain high-frequency dynamics from hydrogen-related energy terms in the water molecules. Following equilibration, well-tempered metadynamics was used to study the free energy landscape of the ligands. The simulations are performed using a LAMMPS patch with the PLUMED v2 package.(17, 39) The biased collective variables are the distances between the center of mass of the coordinating nitrogens on each ligand and the metal ion. Gaussian hills with a width of 0.2 Å are added at a rate of 1 kJ/mol for every 500 timesteps to bias the energy and a bias factor of 6 is applied. Simulations are run for 200 ns and convergence of the landscape is verified (*SI Appendix*, Fig. S10).

**Quantification of Free Energy Landscape Parameters.** Binding energy is calculated from the difference between the free energy of the entire simulated system (ligands, metal ion, water, counterions) where one ligand is bound and the other is dissociated and the lowest well depth in the landscape where all ligands are bound to the metal ion. Activation energy is calculated from the highest peak before dissociation of the ligand from the metal ion. The breaking distance is defined as the maximum bond length between any coordinating nitrogen and $Ni^{2+}$ is 2.11 Å corresponding to a CV distance of ~5 Å for histidine and ~4.5 Å for imidazole. Well width is characterized by a fitting to a Gaussian equation centered at the deepest well.

**Data, Materials, and Software Availability.** All study data are included in the article and/or *SI Appendix*.

**ACKNOWLEDGMENTS.** E.K. would like to acknowledge the NSF Graduate Research fellowship. M.J.B. and E.K. acknowledge support from ARO (W911NF1920098), NIH (U01EB014976 and 1R01AR077793), and ONR (N00014-19-1-2375 and N00014-20-1-2189).

Author affiliations: [a]Department of Materials Science and Engineering, Massachusetts Institute of Technology, Cambridge, MA 02139; [b]Laboratory for Atomistic and Molecular Mechanics, Massachusetts Institute of Technology, Cambridge, MA 02139; and [c]Department of Bioengineering and Department of Materials Science and Engineering, Lehigh University, Bethlehem, PA 18015

1. Matthew J. Harrington, Admir Masic, N. Holten-Andersen, J. H. Waite, P. Fratzl, Iron-clad fibers: A metal-based biological strategy for hard flexible coatings. *Science (80-.).* **328**, 216–220 (2010).
2. C. C. Chou *et al.*, Ion effect and metal-coordinated cross-linking for multiscale design of Nereis jaw inspired mechanomutable materials. *ACS Nano* **11**, 1858–1868 (2017).
3. E. Khare, N. Holten-Andersen, M. J. Buehler, Transition-metal coordinate bonds for bioinspired macromolecules with tunable mechanical properties. *Nat. Rev. Mater.* **6**, 421–436 (2021).
4. N. Holten-Andersen *et al.*, pH-induced metal-ligand cross-links inspired by mussel yield self-healing polymer networks with near-covalent elastic moduli. *Proc. Natl. Acad. Sci. U.S.A.* **108**, 2651–2655 (2011).
5. D. E. Fullenkamp, L. He, D. G. Barrett, W. R. Burghardt, P. B. Messersmith, Mussel-inspired histidine-based transient network metal coordination hydrogels. *Macromolecules* **46**, 1167–1174 (2013).
6. S. C. Grindy *et al.*, Control of hierarchical polymer mechanics with bioinspired metal-coordination dynamics. *Nat. Mater.* **14**, 1210–1216 (2015).
7. B. P. Lee, S. Konst, Novel hydrogel actuator inspired by reversible mussel adhesive protein chemistry. *Adv. Mater.* **26**, 3415–3419 (2014).
8. A. Walther, Viewpoint: From responsive to adaptive and interactive materials and materials systems: A roadmap. *Adv. Mater.* **32**, 1905111 (2020).
9. Z. Xu, Mechanics of metal-catecholate complexes: The roles of coordination state and metal types. *Sci. Rep.* **3**, 2914 (2013).
10. Y. Vidavsky *et al.*, Tuning the mechanical properties of metallopolymers via ligand interactions: A combined experimental and theoretical study. *Macromolecules* **53**, 2021–2030 (2020).
11. Q. Daniel *et al.*, Rearranging from 6- to 7-coordination initiates the catalytic activity: An EPR study on a Ru-bda water oxidation catalyst. *Coord. Chem. Rev.* **346**, 206–215 (2017).
12. W. Sun *et al.*, Molecular engineering of metal coordination interactions for strong, tough, and fast-recovery hydrogels. *Sci. Adv.* **6**, eaaz9531 (2020).
13. S. C. Grindy, M. Lenz, N. Holten-Andersen, Engineering elasticity and relaxation time in metal-coordinate cross-linked hydrogels. *Macromolecules* **49**, 8306–8312 (2016).
14. G. A. Parada, X. Zhao, Ideal reversible polymer networks. *Soft Matter* **14**, 5186–5196 (2018).
15. W. C. Yount, D. M. Loveless, S. L. Craig, Strong means slow: Dynamic contributions to the bulk mechanical properties of supramolecular networks. *Angew. Chem. Int. Ed. Engl.* **44**, 2746–2748 (2005).
16. A. Barducci, G. Bussi, M. Parrinello, Well-tempered metadynamics: A smoothly converging and tunable free-energy method. *Phys. Rev. Lett.* **100**, 020603 (2008).
17. M. Bonomi *et al.*, PLUMED: A portable plugin for free-energy calculations with molecular dynamics. *Comput. Phys. Commun.* **180**, 1961–1972 (2009).
18. P. Tiwary, M. Parrinello, From metadynamics to dynamics. *Phys. Rev. Lett.* **111**, 230602 (2013).
19. S. A. Cazzell, N. Holten-Andersen, Expanding the stoichiometric window for metal cross-linked gel assembly using competition. *Proc. Natl. Acad. Sci. U.S.A.* **22**, 201906349 (2019).
20. C. N. Z. Schmitt, Y. Politi, A. Reinecke, M. J. Harrington, Role of sacrificial protein-metal bond exchange in mussel byssal thread self-healing. *Biomacromolecules* **16**, 2852–2861 (2015).
21. T. Rossow, A. Habicht, S. Seiffert, Relaxation and dynamics in transient polymer model networks. *Macromolecules* **47**, 6473–6482 (2014).
22. C. C. Broomell, S. F. Chase, T. Laue, J. H. Waite, Cutting edge structural protein from the jaws of Nereis virens. *Biomacromolecules* **9**, 1669–1677 (2008).
23. R. K. Khan, P. K. Stoimenov, T. E. Mates, J. H. Waite, G. D. Stucky, Exploring gradients of halogens and zinc in the surface and subsurface of Nereis jaws. *Langmuir* **22**, 8465–8471 (2006).
24. E. Degtyar, M. J. Harrington, Y. Politi, P. Fratzl, The mechanical role of metal ions in biogenic protein-based materials. *Angew. Chem. Int. Ed.* **53**, 12026–12044 (2014).
25. D. U. Ferreiro, E. A. Komives, P. G. Wolynes, Frustration in biomolecules. *Q. Rev. Biophys.* **47**, 285–363 (2014).
26. P. Li, K. M. Merz, Metal ion modeling using classical mechanics. *Chem. Rev.* **117**, 1564–1686 (2017).
27. P. Zhang, J. Han, P. Cieplak, M. S. Cheung, Determining the atomic charge of calcium ion requires the information of its coordination geometry in an EF-hand motif. *J. Chem. Phys.* **154**, 124104 (2021).
28. J. Kahlen, L. Salimi, M. Sulpizi, C. Peter, D. Donadio, Interaction of charged amino-acid side chains with ions: An optimization strategy for classical force fields. *J. Phys. Chem. B* **118**, 3960–3972 (2014), 10.1021/jp412490c.
29. P. Hänggi, P. Talkner, M. Borkovec, Reaction-rate theory: Fifty years after Kramers. *Rev. Mod. Phys.* **62**, 251–341 (1990).
30. S. Tang, B. D. Olsen, Relaxation processes in supramolecular metallogels based on histidine-nickel coordination bonds. *Macromolecules* **49**, 9163–9175 (2016).
31. S. Tang, A. Habicht, S. Li, S. Seiffert, B. D. Olsen, Self-diffusion of associating star-shaped polymers. *Macromolecules* **49**, 5599–5608 (2016).
32. S. Plimpton, Fast parallel algorithms for short-range molecular dynamics. *J. Comput. Phys.* **117**, 1–19 (1995).
33. A. D. MacKerell *et al.*, All-atom empirical potential for molecular modeling and dynamics studies of proteins. *J. Phys. Chem. B* **102**, 3586–3616 (1998).
34. A. D. Mackerell, M. Feig, C. L. Brooks, Extending the treatment of backbone energetics in protein force fields: Limitations of gas-phase quantum mechanics in reproducing protein conformational distributions in molecular dynamics simulation. *J. Comput. Chem.* **25**, 1400–1415 (2004).
35. C. S. Babu, C. Lim, Empirical force fields for biologically active divalent metal cations in water. *J. Phys. Chem. A* **110**, 691–699 (2006).
36. H. Lee, R. M. Venable, A. D. MacKerell, R. W. Pastor, Molecular dynamics studies of polyethylene oxide and polyethylene glycol: Hydrodynamic radius and shape anisotropy. *Biophys. J.* **95**, 1590–1599 (2008).
37. R. W. Hockney, J. W. Eastwood, *Computer Simulation Using Particles* (Taylor and Francis Group, 1988).
38. H. C. Andersen, Rattle: A "velocity" version of the shake algorithm for molecular dynamics calculations. *J. Comput. Phys.* **52**, 24–34 (1983).
39. G. A. Tribello, M. Bonomi, D. Branduardi, C. Camilloni, G. Bussi, PLUMED 2: New feathers for an old bird. *Comput. Phys. Commun.* **185**, 604–613 (2014).
40. I. M. Rasid, J. Ramirez, B. D. Olsen, N. Holten-Andersen. Understanding the molecular origin of shear thinning in associative polymers through quantification of bond dissociation under shear. *Physical Review Materials* **4**, 055602 (2020).